KeAi
CHINESE ROOTS
GLOBAL IMPACT

Available online at www.keaipublishing.com/en/journals/journal-of-magnesium-and-alloys/

ScienceDirect

Journal of Magnesium and Alloys 13 (2025) 1088–1098

www.elsevier.com/locate/jma

Full Length Article

Understanding pyramidal slip-induced deformation bands and dynamic recrystallization in AZWX3100 magnesium alloy

Risheng Pei*, Fatim-Zahra Mouhib, Mattis Seehaus, Simon Arnoldi, Pei-Ling Sun, Talal Al-Samman

Institute for Physical Metallurgy and Materials Physics, RWTH Aachen University, 52074, Aachen, Germany

Received 28 November 2024; received in revised form 24 January 2025; accepted 5 February 2025
Available online 6 March 2025

Abstract

Dynamic recrystallization (DRX) in inhomogeneous deformation zones, such as grain boundaries, shear bands, and deformation bands, is critical for texture modification in magnesium alloys during deformation at elevated temperatures. This study investigates the DRX mechanisms in AZWX3100 magnesium alloy under plane strain compression at 200 °C. Microstructural analysis revealed necklace-type DRX accompanied by evidence of local grain boundary bulging. Additionally, ribbons of recrystallized grains were observed within fine deformation bands, aligned with theoretical pyramidal I and II slip traces derived from the matrix. The distribution of local misorientation within the deformed microstructure demonstrated a clear association between deformation bands and localized strain. Dislocation analysis of lamellar specimens extracted from two pyramidal slip bands revealed $<c + a>$ dislocations, indicating a connection between $<c + a>$ slip activation and the formation of deformation bands. Crystal plasticity simulations suggest that the orientation of deformation bands is responsible for the unique recrystallization texture of the DRX grains within these bands. The texture characteristics imply a progressive, glide-induced DRX mechanism. A fundamental understanding of the role of deformation bands in texture modification can facilitate future alloy and process design.

Keywords: Magnesium; Channel die; Dynamic recrystallization; Texture modification; Pyramidal slip.

1. Introduction

The modern industry increasingly demands advanced materials that are specifically tailored to meet precise technical requirements. As a result, extensive research is focused on gaining a deep understanding of material microstructures. In the manufacturing of sheet metal components, which are utilized across nearly every industrial sector, fundamental processes such as deformation and recrystallization play crucial roles in determining the final microstructure and properties of the materials. This is especially important for magnesium alloys, which are preferred for weight reduction due to their low density and high strength. However, these alloys present challenges due to their asymmetric yielding behavior and limited formability at room temperature, making it difficult to produce high-performance, defect-free parts [1–3].

Various strategies have been employed to address these challenges, with a primary focus on modifying the strong basal-type texture that results from the preferred alignment of basal planes parallel to the principal direction of material flow during rolling or extrusion. In this context, static recrystallization during annealing has proven effective in altering the texture of magnesium alloys, particularly those containing dilute solute additions such as Zn and rare earth elements or Zn and Ca [4–8]. During hot deformation at approximately $0.4T_m$ (where T_m is the melting temperature in K), the material often undergoes DRX. This process changes the grain size and crystallographic orientation while reducing dislocation density. The resulting softening effect decreases the flow

* Corresponding author.
E-mail address: pei@imm.rwth-aachen.de (R. Pei).

https://doi.org/10.1016/j.jma.2025.02.013

stress and has the potential to promote strain localization in the DRX fraction by varying the strength distribution within the deformed volume.

DRX is typically influenced by various factors, including deformation conditions, pre-strain, initial grain size, solute concentration, and the presence of second phase precipitates [9,10]. From an intrinsic perspective, the stacking fault energy (SFE) plays a significant role in DRX because it affects how unit dislocations dissociate into partial dislocations. The width of the stacking fault influences the degree of dynamic recovery and ultimately determines the type of DRX that occurs during hot deformation. In this context, DRX mechanisms can be categorized into two main types: those involving grain boundary migration or subgrain rotation [11,12]. DRX via these mechanisms is termed discontinuous (DDRX) and continuous dynamic recrystallization (CDRX), respectively.

DDRX typically begins at pre-existing high-angle boundaries, especially in materials with low SFE. In these cases, new strain-free grains nucleate and grow at the expense of the deformed microstructure [9,13]. Conversely, in materials with high SFE, facilitated climb and cross-slip of perfect dislocations enhance dynamic recovery. This process rearranges the dislocation structure into lower-energy configurations, reducing the driving force for DDRX [9,13]. Consequently, new DRX grains form via CDRX within the original deformed grains. This mode involves minimal boundary migration as subgrains gradually increase their sub-boundary misorientation until high-angle boundaries develop [9,13].

The DRX mode in magnesium is influenced by the anisotropy of the SFE between different crystallographic planes. The basal planes have a relatively low SFE, around 36 mJ/m^2 [14], while the prismatic and pyramidal planes exhibit much higher SFE values, at 265 and 344 mJ/m^2, respectively [14]. The higher SFE associated with prismatic and pyramidal planes facilitates CDRX. In contrast, the low SFE of basal planes hinders dynamic recovery, leading to enhanced strain hardening, which increases the driving force for DDRX, especially when solutes are present [15]. By adjusting deformation temperature and strain rate, these two DRX modes can either operate concurrently or sequentially [16–18]. The resulting recrystallization texture is determined by the orientation of newly formed grains and the competition between their nucleation and growth rates. Whether the initial deformation texture is retained or eliminated during recrystallization depends on whether substantial recovery and polygonization occur or if newly oriented grains begin to dominate the process.

In this study, we investigate DRX in a complex AZWX3110 magnesium alloy subjected to plane strain compression at 200 °C. This alloy, derived from the commonly used AZ31B, includes micro-additions of calcium (Ca) and yttrium (Y) to tailor its microstructure and texture for enhanced strength and formability [19]. The presence of aluminum (Al) causes yttrium to be stripped from the solid solution, forming fine Al_2Y and Al_8Mn_4Y precipitates that enhance the alloy's strength [19]. Additionally, calcium influences unique texture behavior during recrystallization by co-segregating with zinc (Zn) and aluminum at grain boundaries [19]. Both second-phase precipitation and solute segregation impede dislocation movement and high-angle boundary mobility through drag effects. Consequently, they slow down softening processes and increase the fraction of microstructural inhomogeneities such as deformation and shear bands. These factors have significant implications for the type of DRX nucleation mechanism that occurs. As revealed in our results, microstructure characterization of deformed samples up to large strains uncovered distinct bands of dynamically recrystallized grains. Remarkably, even under an immense strain of 100%, DRX remained incomplete. The resulting microstructure exhibited large areas of unrecrystallized grains, contrary to what might be expected for such a high degree of deformation. The focus of this work is on elucidating the DRX behavior of the investigated alloy, with further discussions on how deformation modes and dislocation structures contribute to these observations.

Table 1
Chemical composition of the AZWX3310 alloy (wt.%).

Al	Zn	Mn	Ca	Y	Mg
2.72	0.95	0.40	0.29	0.94	Bal.

2. Experimental procedure

The investigated AZWX3110 alloy was produced through induction melting at 500 mbar under a protective gas atmosphere of Ar/CO_2. Prior to casting, AZ31B alloy, Mg-30Ca master alloy, and pure Y were melted together and homogenized at 800 °C for a short period. Casting took place at 750 °C into a preheated steel mold with dimensions 50 mm × 50 mm × 150 mm, which was coated with a thin layer of BN/Al_2O_3 to facilitate release. Following casting, the alloy underwent a homogenization treatment at 420 °C for 16 h under an argon atmosphere to ensure uniform distribution of elements. This was followed by water quenching to freeze in the microstructure achieved during homogenization. To determine the actual chemical composition of the produced alloy, inductively coupled plasma optical emission spectroscopy (ICP-OES) was employed. The detailed composition is provided in Table 1.

Deformation samples with dimensions of 12 mm × 10 mm × 6 mm were prepared from the cast AZWX3110 material using electrical discharge machining for plane strain compression (PSC) tests. These tests were conducted at 200 °C under a constant strain rate of 10^{-3} s^{-1}, reaching strain levels of 50% and 100%. The deformation was performed using a conventional screw-driven testing machine (ZWICK). By the use of a channel-die, deformation occurred only in the compression (CD) and elongation directions (ED), while it was constrained in the transverse direction (TD). The frictional resistance imposed by the channel walls was reduced by the use of boron nitride as a lubricant. Samples for electron backscatter diffraction (EBSD) mappings were prepared by conventional grinding and mechanical polishing with ethanol-based diamond paste,

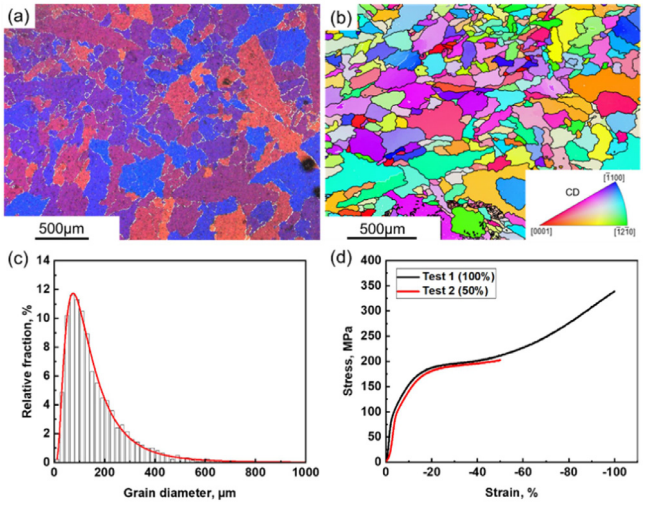

Fig. 1. Microstructure of the cast and homogenized AZWX3110 alloy characterized by (a) optical microscopy and (b) inverse pole figure orientation map with respect to the compression direction of the PSC tests. (c) Grain size distribution. (d) True stress-strain curves during the PSC tests at 200 °C and 10^{-3} s^{-1} strain rate. The strains investigated were 50% and 100%.

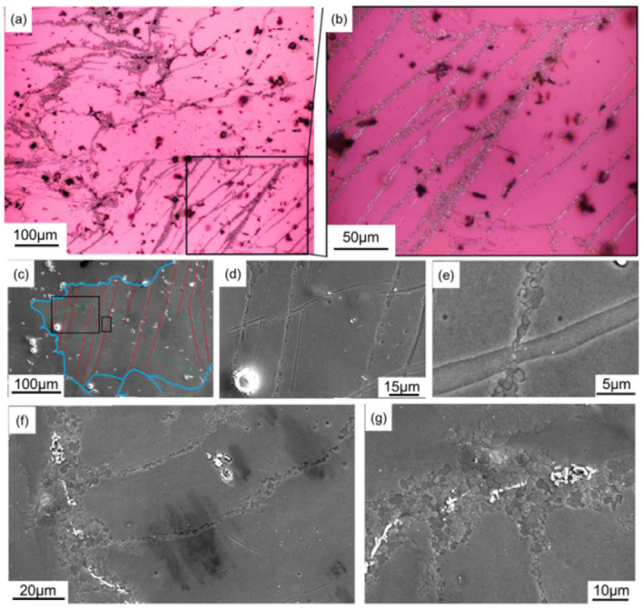

Fig. 2. Optical (a, b) and scanning electron microscopy (SEM) micrographs (c-g) of AZWX3110 deformed in PSC at 200 °C and 10^{-3} s^{-1} to $\boldsymbol{\varepsilon_t} = -0.5$. (c) Example of a deformed grain featuring grain boundary bulging, twins (green) and DRX bands (red). These last two features are visible in the magnified images (d and e) of the rectangle areas in (c). DRX at prior grain boundaries forming a necklace-type structure is illustrated in (f) and (g). (For interpretation of the references to color in this figure legend, the reader is referred to the web version of this article.).

as well as electropolishing in a Struers AC-2 reagent (at 20 V and −20 °C for 90 s). EBSD measurements were carried out using an FEI Helios 600i dual-beam microscope operated at 20 kV, with step sizes below 2 μm. The collected EBSD data was analyzed using the MTEX toolbox [20] to gain insights into the microstructural characteristics of the deformed samples.

Site-specific lamellae for transmission electron microscopy (TEM) analyses were extracted from selected positions identified in the EBSD maps. These lamellae were subsequently thinned using focused ion beam (FIB) milling. The milling procedure involved a stepwise reduction of the beam current until the lamellae reached a final thickness of less than 100 nm. Transmission Kikuchi diffraction (TKD) mapping was conducted on lamellae with a thickness of about 300 nm under a voltage of 30 kV in the FIB machine. This mapping was used to reveal the orientation characteristics of both recrystallized and deformed grains. TEM observations were carried out using a JEOL JEM-F200 equipped with a double tilt holder, operating at an acceleration voltage of 200 kV. For dislocation analysis, different zone axes and various two-beam diffraction conditions were employed. Burgers vector analysis was performed using the g·b invisibility criterion, where g is the diffraction vector and b is the Burgers vector, to gain insights into dislocation structures within the material.

3. Results

3.1. Initial condition

The microstructure of the cast and homogenized material prior to the PSC tests was characterized by optical and orientation microscopy, as depicted in Fig. 1a and b. The data reveal a coarse microstructure with random grain orientations, typical of the as-cast condition. The grain size distribution, determined through the linear intercept method applied to multiple optical images, is shown in Fig. 1c. Grain sizes ranged from 20 to 600 μm, with an average size of approximately 100 μm. Fig. 1d illustrates the stress-strain response during PSC at 200 °C and a strain rate of 10^{-3} s^{-1}, up to logarithmic (true) strains of 50% and 100%, defined by $\varepsilon_t = \ln(1+\varepsilon)$. The two curves display representative flow behavior, characterized by plastic yielding at approximately 80 MPa and work hardening up to around 180 MPa. The subsequent rapid increase in stress is attributed to significant frictional effects that become prominent after strains of about 40%.

3.2. Microstructure evolution at $\varepsilon_t = -0.5$

Microstructure characterization of the deformed sample up to $\varepsilon_t = -0.5$ revealed the presence of fine DRX grains located at prior grain boundaries and within narrow deformation bands of less than 10 μm in width (Fig. 2a). This feature is more clearly illustrated in Fig. 2b. Further examination using SEM indicated the presence of deformation twinning in some grains and serrated grain boundaries in unrecrystallized grains, likely due to local migration of boundary segments. An example is provided in Fig. 2c, where a coarse grain has been selected, to demonstrate parallel bands of DRX grains (highlighted in red), thin lenticular twins (highlighted in green), and a serrated grain boundary with evidence of bulging (outlined in blue). The unrecrystallized twins and the DRX structure associated with the bands are more visible in

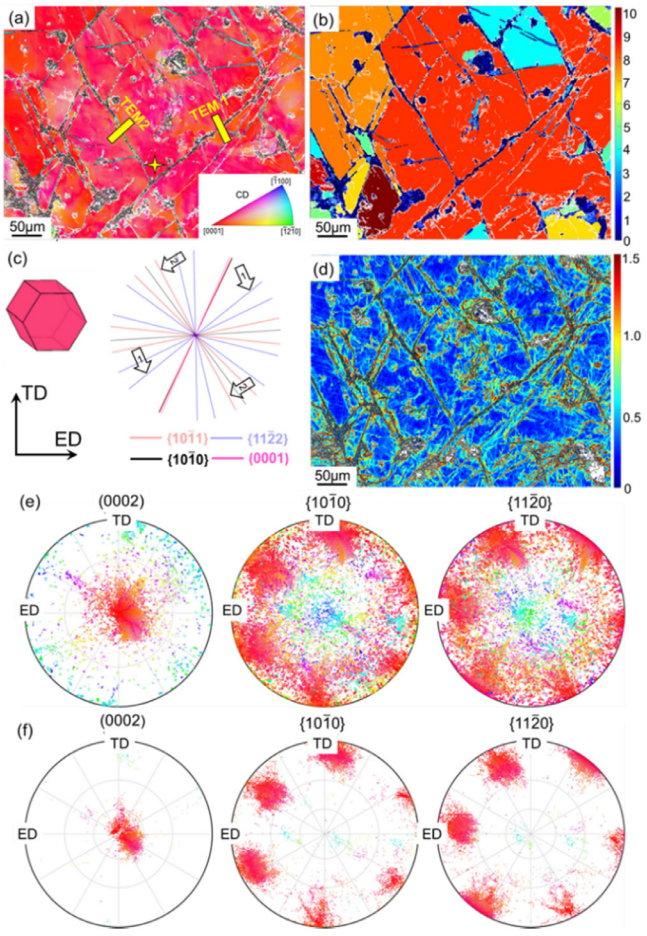

Fig. 3. EBSD analysis of AZWX3110 deformed in PSC at 200 °C and 10^{-3} s^{-1} to $\varepsilon_t = -0.5$. (a) CD-IPF orientation map, with a star marking the average matrix orientation for slip traces in (c), and rectangles indicating TEM lift-out positions shown in Figs. 7 and 8. (b) GOS map identifying recrystallized material with GOS < 1°. (c) Theoretical slip traces of (0001), {10$\bar{1}$0}, {10$\bar{1}$1} and {11$\bar{2}$2} planes from the average matrix orientation; arrows indicate traces parallel to DRX bands used for TEM samples. (d) KAM map showing local misorientation distribution as a qualitative strain metric. (e-f) Scatter pole figures of DRX grains (GOS < 1°) and deformed matrix orientations, color-coded by CD-IPF.

the magnified images of the outlined areas (black rectangles) within the selected grain, as seen in Fig. 2d and e. By observing the intersection between a twin and a DRX band in Fig. 2e, it can be inferred that twins formed initially in the coarse-grained microstructure, preceding both band formation and recrystallization at higher strain. From Fig. 2f and g, it is apparent that the bands filled with DRX grains originate at the grain boundary and propagate within the grain interior, traversing to the opposite side.

To investigate the development of grain orientations after deformation, representative EBSD measurements (450 μm × 350 μm) were performed in the mid TD-ED-section. Fig. 3 presents the resulting EBSD data, featuring an IPF orientation map with respect to CD (Fig. 3a), grain orientation spread (GOS) map (Fig. 3b) and a fourth-order kernel average misorientation (KAM) map (Fig. 3d). The sampled area displays multiple parallel bands aligned in two main directions relative to the sample axes. The prominent red color in the IPF map indicates the development of a basal texture in the sample during PSC deformation, characterized by a notable alignment of the c-axes of deformed grains with the CD. The discernible gradients in the color coding (red – orange – purple) in the map signify a texture scatter of approximately 35° around the CD.

Theoretical slip traces on {0001}, {10$\bar{1}$0}, {10$\bar{1}$1}, and {11$\bar{2}$2} planes relative to the matrix orientation (indicated by a yellow star in Fig. 3a) reveal that the observed bands are aligned parallel to pyramidal first ({10$\bar{1}$1}) and second ({11$\bar{2}$2}) order planes, respectively (Fig. 3c). In Fig. 3b, DRX grains within these bands appear as regions with lower values of orientation spread (<1°), whereas the surrounding deformed matrix exhibits higher GOS values, reaching up to 10°. In this context, using GOS as a metric for intragranular misorientation analysis is beneficial for visualizing recrystallized domains within a deformed microstructure. [19,21,22].

The KAM map depicted in Fig. 3d illustrates the distribution of local lattice distortion and stored energy within the deformed microstructure, clearly highlighting the association of deformation bands with localized strain. The non-indexed narrow regions within these bands display the highest local strain, while other areas in the matrix, such as grain interiors, experience less strain and exhibit a notably higher degree of homogeneous deformation. The orientation distributions of the DRX grains and the deformed grains, based on their GOS values, are represented in Fig. 3e and f in terms of (0001), {10$\bar{1}$0} and {11$\bar{2}$0} EBSD pole figures with CD-IPF coloring. The deformed portion of the microstructure exhibits a well-defined basal texture of the type (0001)//CD-{11$\bar{2}$0}//ED (Fig. 3f). In contrast, the texture of the DRX grains appears to consist partly of orientations inherited from the surrounding deformed matrix, along with new off-basal orientations marked by a significant c-axis tilt from the CD. These new orientations broaden the available orientation spectrum for the microstructure undergoing PSC deformation, thereby weakening the strong basal texture characteristic of the matrix.

3.3. Microstructure evolution at $\varepsilon_t = -1$

As the deformation increased to 100%, there was a notable rise in the occurrences of twins and the DRX fraction. Fig. 4a presents a representative optical micrograph of a sample compressed to 100% at 200 °C and 10^{-3} s^{-1}. A selected region was examined at higher magnification to better visualize deformation twins and recrystallized bands, which appeared coarser compared to those observed at 50% deformation. In this context, either the DRX grain size within the band interior increased (Fig. 4b), or the band itself consisted of several ribbons of fine DRX grains (Fig. 4d). Similar to lower deformation strains, new twins were observed originating from these recrystallized bands, as shown in Fig. 4b and d. Interestingly, as illustrated in Fig. 4e, the primary nucleated twin was evidently sheared by the DRXed band.

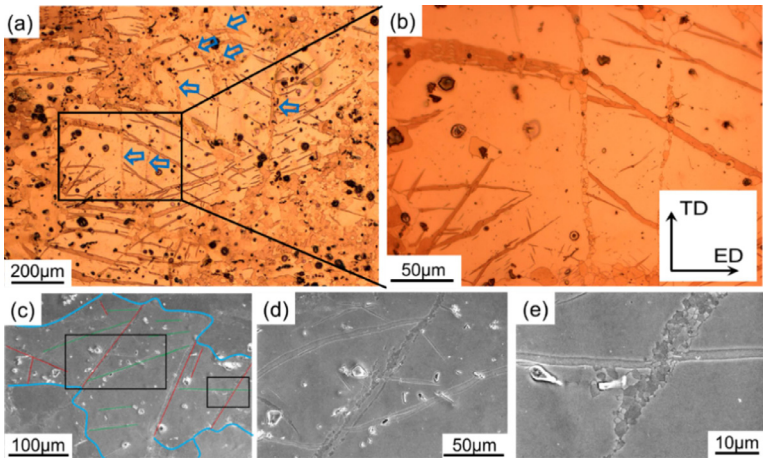

Fig. 4. Optical (a,b) and SEM (c-e) micrographs of AZWX3110 deformed in PSC at 200 °C and 10^{-3} s^{-1} to $\varepsilon_t = -1$. The insets in (a) and (c) are reproduced at higher magnifications to improve the visibility of DRX sites and their characteristics at this strain level; arrows in (a) indicate several examples of DRX bands.

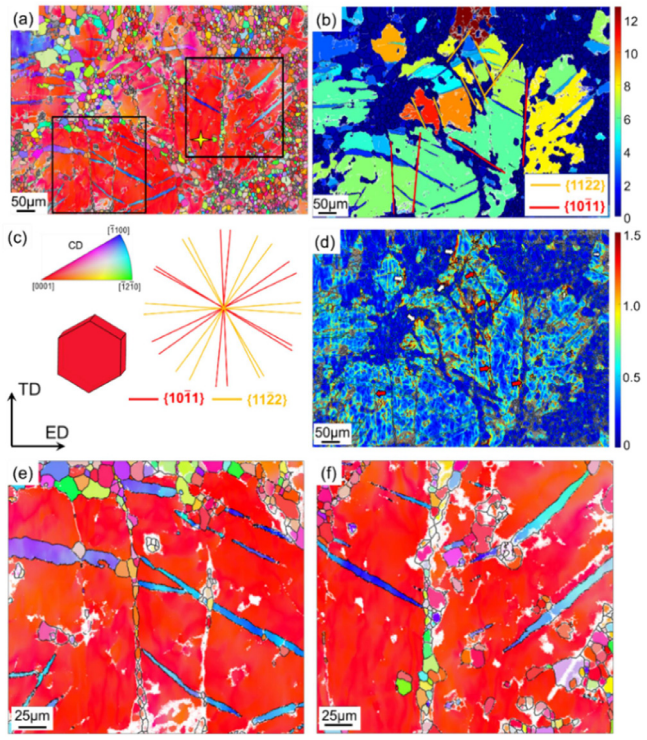

Fig. 5. EBSD analysis of AZWX3110 deformed in PSC at 200 °C and 10^{-3} s^{-1} to $\boldsymbol{\varepsilon_t} = -1$. (a) CD-IPF map with a star indicating the average matrix orientation for slip traces in (b) and (c). (b) GOS map identifying recrystallized material with GOS < 1°. (c) Slip traces of {10$\bar{1}$1} and {11$\bar{2}$2} planes from the average matrix orientation. (d) KAM map showing localized strain distribution. (e-f) Magnified CD-IPF maps of areas in (a), highlighting heterogeneous DRX nucleation sites linked to local stress concentrations and lattice distortion in adjacent poorly-indexed regions.

The orientation analysis carried out by EBSD is presented in Fig. 5, showing an increase in both the size and fraction of recrystallized grains compared to the lower strain condition of 50%. The off-basal orientations of DRX grains are not confined to specific nucleation sites, as both recrystallized bands and grain boundaries display a wide range of orientations. Notably, the visible {10$\bar{1}$2} extension twins remain unrecrystallized, identifiable by their IPF color (blue) relative to the matrix (red) (Fig. 5a). A clearer depiction of the distribution of the DRX structure relative to the parent matrix is presented in the GOS map, which highlights internal misorientations of less than 1°. Furthermore, the {10$\bar{1}$2} extension twins exhibit low GOS values ranging from 1° to 3°, while their parent grains display internal misorientations up to 9° (Fig. 5b). The dashed lines in the GOS map highlight the alignment of visible DRX bands with {10$\bar{1}$1} and {11$\bar{2}$2} pyramidal slip traces shown in Fig. 5c. These traces are referenced to a point marked by a yellow star in the IPF map, representing the average matrix orientation.

The spread of KAM values in the DRX and deformed regions is depicted in Fig. 5d. The recrystallized grains exhibit low KAM values (~0.2°), consistent with the typical angular resolution of EBSD, confirming their nearly dislocation-free nature. In contrast, the deformed areas display evident gradients in dislocation density and associated stored energy. Interestingly, higher KAM values in the map correlate with (i) the DRX bands, as demonstrated earlier in Fig. 3 (indicated by red arrows in Fig. 5d), and (ii) other grain boundary regions adjacent to DRX structures (highlighted by white arrows). In these areas, many recrystallized grains develop protrusions towards neighboring regions with high KAM values, promoting DRX progression at the expense of local variations in dislocation density.

The comparatively lower KAMs (< 0.5°) within some deformed grain interiors are likely due to dynamic recovery and a reduction in dislocation density. Closer observations were made in two areas marked with rectangles in Fig. 5a, with CD-IPF maps presented in Fig. 5e and f. Notably, small recrystallized nuclei form along lines of low-angle grain boundaries in Fig. 5e. The grain near the intersection point with twins is significantly larger than others, possibly due to

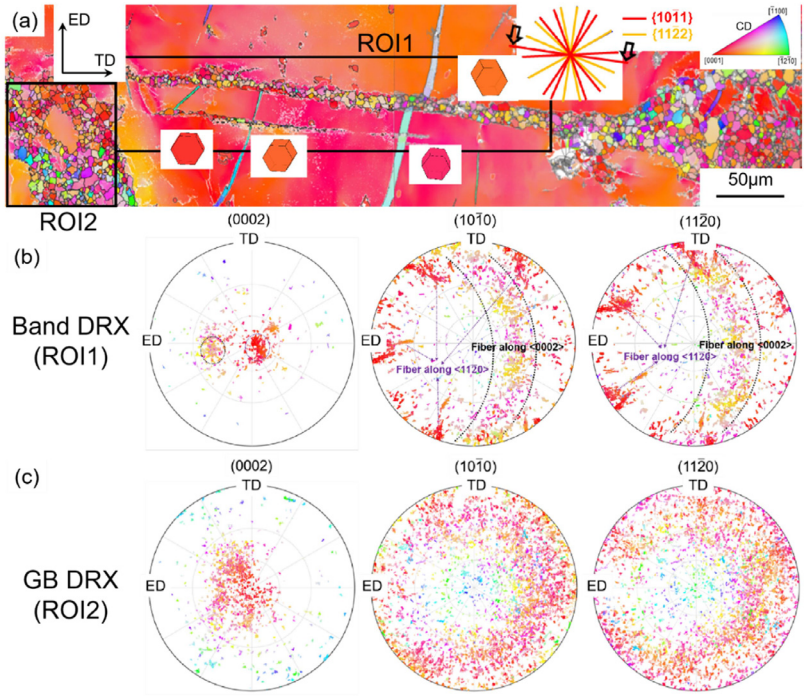

Fig. 6. EBSD mapping of DRX orientations in AZWX3110 deformed in PSC at 200 °C and 10^{-3} s^{-1} to $\varepsilon_t = -1$: (a) IPF map showing recrystallized grains within a deformation band and along a grain boundary, with pyramidal plane slip traces indicated; (b) DRX associated with deformation bands (ROI 1); (c) DRX related to grain boundaries (ROI 2). The color coding corresponds to CD-IPF.

dislocation pile-up on twin boundaries as deformation bands propagate through them. These findings suggest that dynamic recrystallization is initiated with the aid of a dislocation density gradient.

A detailed analysis of the orientations of nuclei within the recrystallized band revealed that specific texture components originated from the band nucleation. Fig. 6a show CD-IPF maps of a nuclei-rich recrystallized band intersecting twins. The continuity of the recrystallization band through the intersected twin, as well as significant shearing of the twin along the band direction, is evident. Comparing the band direction to theoretical traces of $\{10\bar{1}1\}$ and $\{11\bar{2}2\}$ pyramidal planes relative to the matrix orientation in Fig. 6a shows clear alignment with the pyramidal first order plane $\{10\bar{1}1\}$. The unit cells of the orientations in the matrix on both sides of the recrystallized bands are included in Fig. 6a. The top part of the grain aligns its c-axis to the right, while the bottom side aligns it to the left, indicating different deformation and lattice misfits within the grain and highlighting the necessity for a deformation band. Additionally, according to the color key, there is a distinct difference in orientation between recrystallized grains, both inside and at grain boundaries (off-basal), and those in the deformed matrix (basal).

The CD-IPF maps in Figs. 5 and 6 provide a view of the developed DRX orientations at $\varepsilon_t = -1$. The microstructures primarily highlight favorable recrystallization sites within bands of refined grains (Fig. 6a), at intersection points with $\{10\bar{1}2\}$ twins, and near second phase particles within the grain interior, where EBSD indexing was not possible (Fig. 5e-f). The impact of DRX on texture randomization is evident through the diverse orientations emerging from the nucleation and growth of recrystallized grains at these sites. In Fig. 6b and c, EBSD scatter pole figures depict the orientations of recrystallized grains associated with deformation band nucleation (ROI 1) and grain boundary nucleation (ROI 2), respectively. Unlike the distinct basal orientation in the matrix, ROI 1 exhibits two orientation fibers along $<11\bar{2}0>$ and $\langle 0002\rangle$. The fiber along $<11\bar{2}0>$ shows a good agreement with the texture of the deformed matrix (see Fig. 3f), indicating that it originates from the surrounding deformed matrix around the recrystallized band. The second fiber arises from nuclei within the recrystallized band introduced by deformation. In contrast to this well-defined fiber texture, DRX at grain boundaries in ROI 2 presents an almost random-type texture, as shown by large basal pole scatter around CD in Fig. 6c.

4. Discussion

In the as-cast condition prior to PSC, the large average initial grain size (~100 μm) typically leads to fewer nucleation sites due to a reduced grain boundary area. This is likely responsible for the slow recrystallization kinetics, resulting in a significant portion of the microstructure remaining unrecrystallized even at a large strain of −1. Additionally, the low density of nucleation sites may be compounded by solute and/or Zener drag effects in the AZWX3110 alloy, as discussed in [19], which can further impede boundary migration and potentially hinder complete recrystallization. The drag effect from solute species or precipitates might intensify if deformation becomes localized within the DRX fraction of

the material, ultimately reducing the available stored energy at larger strains.

Regarding the deformation behavior, it was observed that materials with a large initial grain size tend to exhibit increased strain localization and the formation of deformation heterogeneities, such as deformation bands and intersecting twins. Once pre-existing grain boundaries are fully decorated with recrystallized grains in a necklace structure, nucleation is exhausted, making deformation bands critical sites for intragranular DRX nucleation. IPF orientation maps derived from EBSD data revealed distinct texture differences between the original large grains and the newly formed recrystallized grains. Unlike the concentration of the c-axis of matrix grains around the CD, DRX grains, particularly those within bands, developed new orientations characterized by basal pole rotations of 35°–55° towards the ED. Interestingly, examination of the corresponding $\{10\bar{1}0\}$ and $\{11\bar{2}0\}$ pole figures revealed that the DRX orientations form a basal fiber due to progressive rotations of respective grains around their c-axes, suggesting a continuous strain-induced process within the DRX bands.

By utilizing GOS and KAM maps, we distinguished recrystallized material from surrounding deformed microstructure. The expansion of the recrystallization front at the expense of adjacent deformed neighbors appears to be driven by local variations in stored dislocation density. This is evident from protruding grain boundary segments migrating towards regions with higher KAM values. Similar findings were reported in a related quasi-in situ EBSD annealing study on deformed AZ31 magnesium alloy [23]. The authors of the study also explored how local curvature influences grain boundary migration kinetics during recrystallization but concluded that dislocation stored energy is the primary driver for this process rather than grain boundary energy.

Upon examining the theoretical slip traces within the matrix, we observed that the recrystallized bands in the deformed microstructures tend to align preferentially with the calculated slip traces of first and second-order pyramidal planes. This suggests a potential relationship between slip system activation and the formation of deformation bands. Due to the initially large grain size at the onset of deformation, there are local variations in the density of gliding basal dislocations within grain interiors, leading to non-uniform operation of primary basal slip. This deformation inhomogeneity can result in different lattice rotations, which in turn cause localized plastic bending of primary slip planes within individual grains. As deformation progresses, the density of excess dislocations increases in regions with local lattice curvature. To alleviate the long-range stress fields that arise, these dislocations reorganize into geometrically necessary boundaries that are perpendicular to the primary slip direction. This process has been documented in the literature to describe the formation of kink bands in fcc materials [24–26], where it has been found that the number of bands increases with ongoing deformation, thereby reducing the slip path of primary dislocations. This reduction is believed to facilitate the activation of secondary slip systems as an additional means of strain accommodation. Stress concentrations caused by primary dislocation pile-ups against the band walls gradually transform these into high-angle boundaries [24,27,28].

In our study, the deformation bands exhibited a clear alignment parallel to the traces of $\{10\bar{1}1\}$ and $\{11\bar{2}2\}$ pyramidal planes, suggesting a possible interaction between primary basal slip and secondary pyramidal slip as a mechanism for their formation. The presence of numerous $\{10\bar{1}2\}$ twins intersected by these deformation bands supports the notion that twins likely formed first due to their low critical resolved shear stress. The bands then emerged later after sufficient accumulation of pyramidal slip at significantly higher local stress levels. Moreover, the ability to intersect and shear pre-existing twins provides further evidence linking deformation bands to dislocation activity.

Further investigations were conducted using transmission electron microscopy (TEM) on selected regions to elucidate the relationship between slip activity, dislocation types, and the formation of deformation bands. Fig. 7 presents a correlative TKD and TEM analysis of a lamella extracted from a recrystallized band parallel to the first-order pyramidal plane $\{10\bar{1}1\}$. Fig. 7a shows a TKD-EBSD map revealing grain orientations within the analyzed lamella. The corresponding bright field (BF) image is shown in Fig. 7b, highlighting part of a recrystallized band spanning several micrometers in width, along with its surrounding matrix. To investigate the dislocation characteristics within the recrystallized material, several grains were analyzed under different two-beam conditions. Specifically, dislocations with a <c> component are visible under $g = 0002$ and g=hki1 diffraction conditions but remain invisible under g=hki0. These are classified as <c + a> type dislocations. Conversely, dislocations can be identified as <a> type if they are visible under both g=hki0 and g=hki1 diffraction conditions but not under $g = 0002$.

Fig. 7c and d show an example of an analyzed DRX grain marked by a red star in Fig. 7b, where diffraction conditions of $g = 0002$ and $g = 01\bar{1}\bar{1}$ were applied, respectively. Both $<a>$ and $<c + a>$ dislocations can be distinguished using g·b analysis, where only dislocations with <c> components are visible under $g = 0002$, while those with both $<a>$ and <c> components appear under $g = 01\bar{1}\bar{1}$. It is clear that all visible dislocations within the recrystallized grain possess Burgers vectors featuring both components, as indicated by yellow and orange arrows. Straight-line dislocations align parallel to the (0001) traces, whereas curved dislocations lie on non-basal planes.

The dislocation density in the matrix was generally too high to allow for a detailed Burgers vector analysis. However, this analysis was feasible in areas directly adjacent to the DRX bands. Fig. 7e and f, obtained from the deformed region marked by a green star, display numerous $<c + a>$ dislocations indicated by orange arrows, captured under a diffraction vector close to $g = 0002$. Fig. 8 presents another combined TKD-TEM investigation of a second lamella extracted from a $\{11\bar{2}2\}$ DRX band. Within the recrystallized grains of approximately 1 μm shown in Fig. 8a and b, the presence of nano-sized particles supports the previously discussed concept

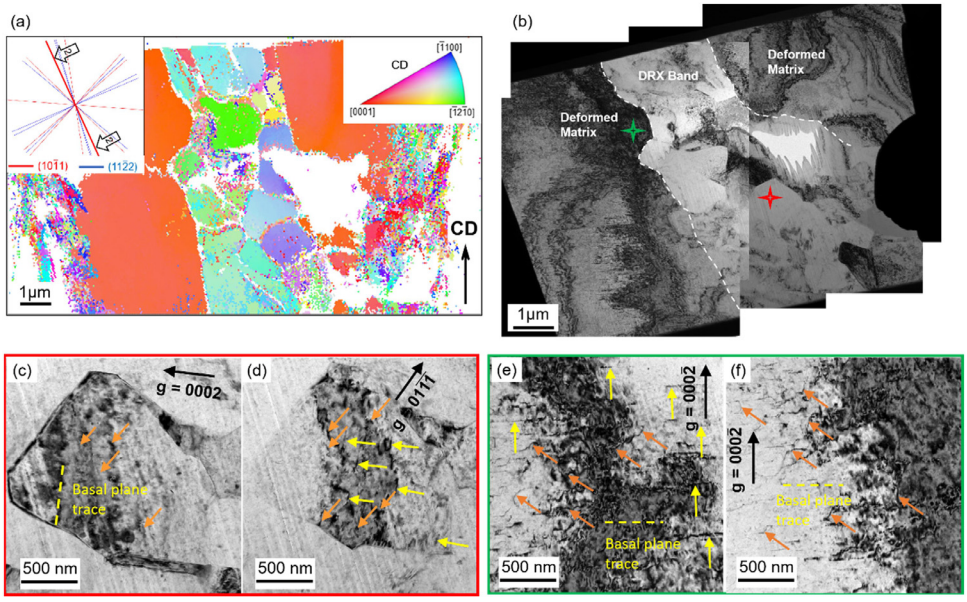

Fig. 7. TEM analysis of the TEM2 lamella from a $\{10\bar{1}1\}$ DRX band and matrix: (a) TKD-EBSD map showing grain orientations with CD-IPF coloring; (b) BF image of the lamella under zone axis $[2\bar{1}\bar{1}0]$, showing the deformed matrix (green star) and DRX band (red star); (c, d) recrystallized grain (red star in b) imaged under $g = 0002$ and $g = 01\bar{1}\bar{1}$ two-beam conditions, showing <c + a> dislocations (orange arrows) visible in both, and <a> dislocations (yellow arrows) visible only in g=$01\bar{1}\bar{1}$; (e, f) deformed region near DRX band (green star), imaged under $g = 000\bar{2}$ condition.

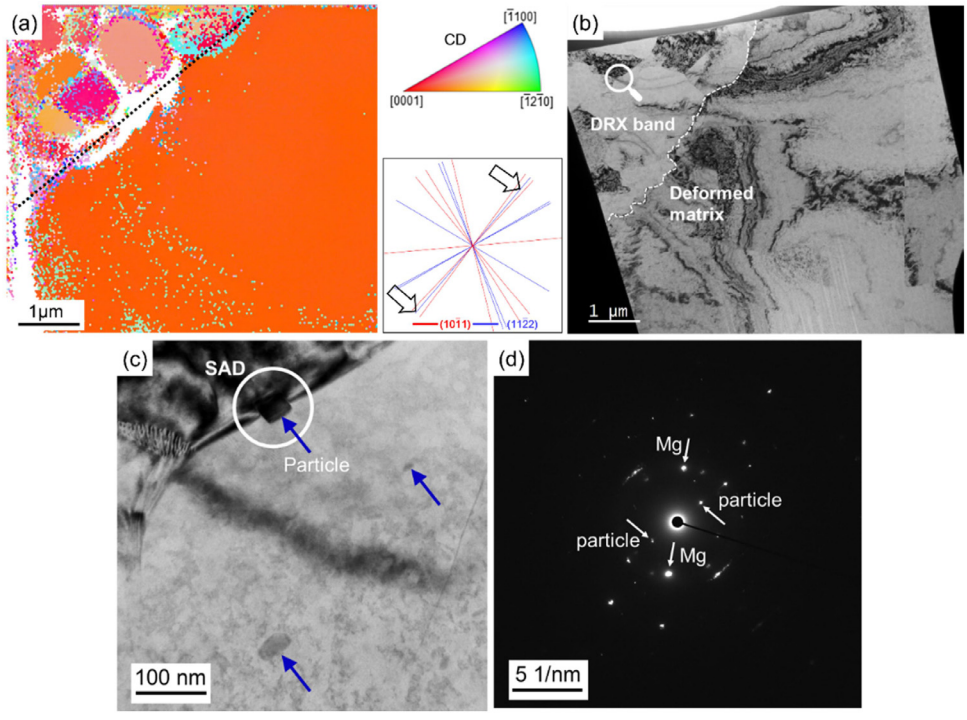

Fig. 8. TEM analysis of TEM1 lamella from a $\{11\bar{2}2\}$ DRX band and matrix. (a) TKD-EBSD map showing orientations of deformed and DRX regions with CD-IPF coloring. (b) BF image of the lamella. (c) Magnified view highlighting nano-sized precipitates (<100 nm) in the recrystallized region. (d) SAD pattern displaying diffraction spots of both the Mg phase and particles.

of drag effects. These particles likely constrain the growth of recrystallized grains, thereby contributing to the stability of DRX bands under higher strain conditions.

The presence of retained $<c + a>$ dislocations within the recrystallized bands and adjacent matrix supports the idea that deformation band formation, prior to recrystallization, is closely linked to $<c + a>$ slip activity on $\{10\bar{1}1\}$ and $\{11\bar{2}2\}$ pyramidal planes under high stress. This involvement suggests a slip transition mechanism between these planes [27,28]. This is particularly notable given reports indicating that solute-enhanced magnesium alloys exhibit increased rates of $<c + a>$ cross-slip [15]. This effect posi-

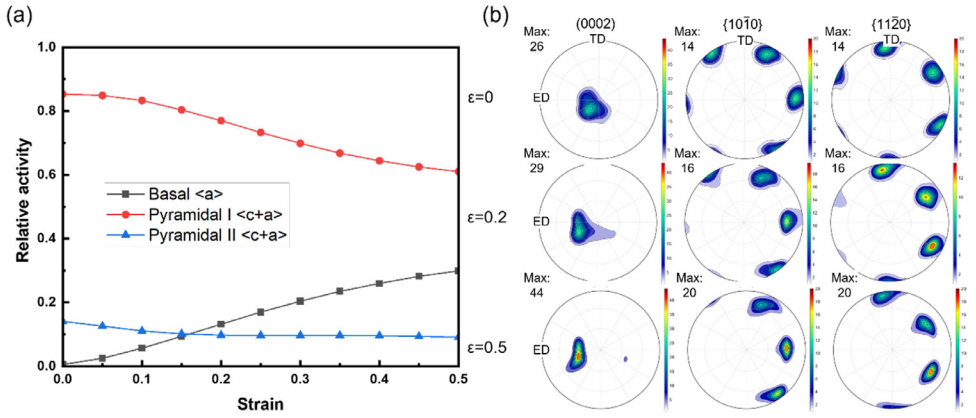

Fig. 9. VPSC crystal plasticity simulation results showing the relative activity of different deformation modes (a) and the resulting texture evolution (b) up to a deformation strain of 0.5.

tively influences their deformation behavior and texture evolution by accommodating strain outside the basal plane. Additionally, enhanced $<c + a>$ cross-slip can help form stable three-dimensional networks of deformation-induced low angle boundaries, crucial for driving CDRX within deformation bands [17].

Previous investigations of the AZWX3110 alloy revealed that Y atoms tend to combine with Al atoms, forming stable Al_2Y precipitates. This is supported by 3D atom probe tomography (APT) findings showing no Y atoms in the matrix or along grain boundaries [19], consistent with other studies [29,30]. In this study, it is thus likely that solute-enhanced $<c + a>$ slip is due to solute Ca rather than Y atoms within the matrix and at grain boundaries. Non-basal slip during PSC deformation facilitates grain rotation towards soft orientations, countering basal texture induced by predominant basal slip and $\{10\bar{1}2\}$ twinning. The off-basal texture component of DRX grains filling $\{10\bar{1}1\}$ and $\{11\bar{2}2\}$ deformation bands likely originate from $<c + a>$ dislocations gliding on these planes. To explore this, simplified crystal plasticity simulations using the viscoplastic self-consistent (VPSC) code [31,32] were conducted to examine whether pyramidal $<c + a>$ slip modes produce similar trends in experimental texture development under deformation and simultaneous DRX (cf. Fig. 6a). The starting texture for the simulations was derived from EBSD data shown in Fig. 6a, excluding the DRX texture component and retaining only the basal orientation of the deformed matrix. Both pyramidal I and II $<c + a>$ slip modes were considered alongside basal slip due to its low critical resolved shear stress (CRSS). Stress-strain data fitting was not performed, and latent hardening (set to 1) along with Voce hardening (set as 0) were not considered during VPSC simulation since the focus was on specific slip system activation and related texture evolution rather than macroscale hardening effects. Based on the PSC strain path, the velocity gradient for simulation was set to $\dot{v}_{33} = -0.001$ *and* $\dot{v}_{22} = 0.001$, with all other components set to zero.

Fig. 9a illustrates the relative activity of slip modes during PSC deformation. Both pyramidal slip modes contribute to plastic deformation from the start, though at different rates. Basal slip increases rapidly with strain, especially as the basal orientation rotates towards the ED (as shown in Fig. 9b), but its contribution remains lower than that of pyramidal I slip. Despite a CRSS ratio of 1 between pyramidal I and II slips, pyramidal II activity is less significant due to its low Schmid factor. The CRSS ratio between basal slip and either pyramidal mode is 1.5. Theoretical studies utilizing molecular dynamics and ab-initio methods often indicate a preference for glide in the pyramidal I plane over the II plane in magnesium, consistent with computed energy barriers and local minima along the slip path [27,33–35]. However, experimental observations of slip traces and TEM dislocation analyses show that both pyramidal I and II $<c + a>$ slips can dominate during c-axis compression of Mg single crystals [36–38] and Mg alloys [35,39–42].

Tang and El-Awady proposed that during c-axis compression, $<c + a>$ dislocations initially nucleate on $\{10\bar{1}1\}$ pyramidal I plane and then cross-slip to $\{11\bar{2}2\}$ pyramidal II planes at higher strain levels [27,35]. Thus, both types coexist with most gliding on $\{11\bar{2}2\}$ planes [27]. Texture simulation results in Fig. 9b indicate a texture transition induced by $<c + a>$ slip as strain increases. The peak position of maximum basal pole density shifts from CD towards ED, leading to the unique <0001> fiber texture component in recrystallized grains within the pyramidal slip bands shown in Fig. 6b.

For a more comprehensive analysis of the ROI 1 texture in Fig. 6, the EBSD scatter data of individual recrystallized orientations within the deformation band was reprocessed into smooth pole figures (Fig. 10a). This enhanced the visualization of texture characteristics. The two prominent texture components of the DRX band were then plotted separately as simulated texture components in Fig. 10b and c. The off-basal component (Fig. 10c) originates from pyramidal $<c + a>$ slip, as previously mentioned. As evident from the prismatic pole figures in Fig. 10c, grains from Mode 1 exhibit a basal fiber, indicating rotational symmetry of $\{10\bar{1}0\}$ and $\{11\bar{2}0\}$ planes along the c-axis (fiber axis). In contrast, another component shares a basal orientation similar to that of the matrix but with noticeable rotation along $<11\bar{2}0>$, as simulated

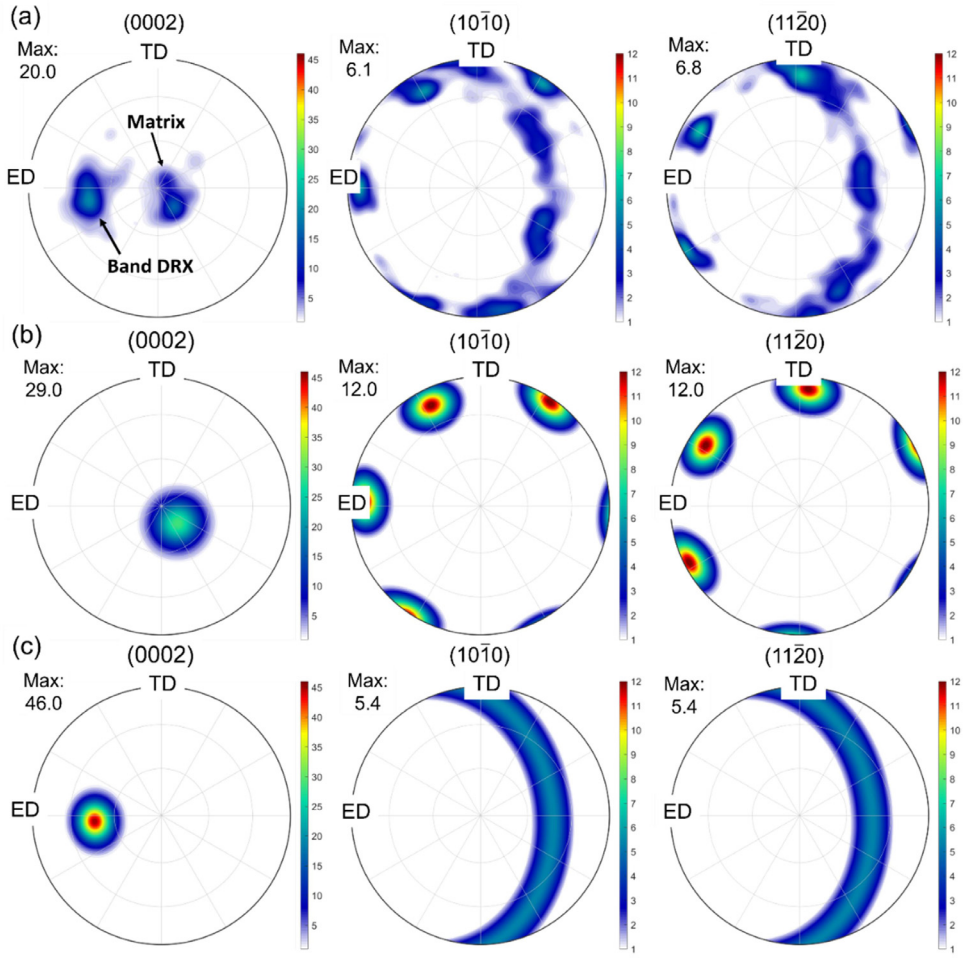

Fig. 10. Texture analysis of the recrystallized grains in the deformation band (ROI 1 in Fig. 6a) of AZWX3110 deformed in PSC at 200 °C and 10^{-3} s^{-1} to $\varepsilon_t = -1$. (a) Measured texture from EBSD map; (b) simulated texture rotated along <11$\bar{2}$0> from an initial orientation of (185°,43°, 171°); (c) simulated texture rotated along ⟨0002⟩ from an initial orientation of (85°,165°, 197°). (For interpretation of the references to color in this figure legend, the reader is referred to the web version of this article.).

in Fig. 10b. These grains share low-angle grain boundaries (LAGB) with the matrix and are located on the edge of the deformation band, as depicted in Fig. 6a and d. This may be related to a sub-grain rotation DRX mechanism [43,44].

5. Conclusions

In this study, as-cast AZWX3100 magnesium alloy with micro-additions of Y and Ca and a large initial grain size was deformed in plane strain compression at 200 °C to explore DRX mechanisms using EBSD and TEM characterization. The conclusions are as follows:

(1) Microstructure analysis revealed necklace-type DRX at serrated grain boundaries and intragranular DRX within fine deformation bands, originating at grain and twin boundaries, aligned with pyramidal I and II slip planes.
(2) EBSD intragranular misorientation analysis showed a link between deformation bands and localized strain, making them favorable DRX sites. Recrystallization progressed with dislocation density variations, forming grains that protrude towards high KAM regions.
(3) TEM dislocation analysis identified abundant $<c + a>$ dislocations in the recrystallized bands and adjacent matrix, underscoring the importance of $<c + a>$ slip in these bands.
(4) Recrystallized grains in the deformation bands exhibited new orientations with basal pole rotations towards the sample's elongation direction. This texture includes a basal fiber component linked to gradual c-axis rotations induced by strain in DRX grains.
(5) Crystal plasticity simulations focusing on predominant pyramidal I and II $<c + a>$ slip confirmed that the unique recrystallization texture of pyramidal slip bands stems from the orientation of deformation bands, suggesting a progressive glide-induced DRX mechanism.

Declaration of interests

The authors declare that they have no known competing financial interests or personal relationships that could have appeared to influence the work reported in this paper.

CRediT authorship contribution statement

Risheng Pei: Writing – original draft, Validation, Methodology, Investigation. **Fatim-Zahra Mouhib:** Writing – review & editing, Investigation. **Mattis Seehaus:** Writing – review & editing, Investigation. **Simon Arnoldi:** Methodology, Investigation. **Pei-Ling Sun:** Methodology, Investigation. **Talal Al-Samman:** Writing – review & editing, Supervision, Project administration, Funding acquisition.

Acknowledgments

The authors gratefully acknowledge funding by the Deutsche Forschungsgemeinschaft (DFG) through projects 420149269, 394480829, and as part of the CRC1394 "Structural and Chemical Atomic Complexity – From Defect Phase Diagrams to Material Properties" (project 409476157).

References

[1] R. Gehrmann, M.M. Frommert, G. Gottstein, Mater Sci Eng A 395 (1–2) (2005) 338–349.
[2] T. Nakata, C. Xu, K. Kaibe, Y. Yoshida, K. Yoshida, S. Kamado, J Magnes Alloy 10 (4) (2022) 1066–1074.
[3] Z. Zhang, J. Xie, J. Zhang, X.-S. Yang, R. Wu, J Magnes Alloy 12 (5) (2024) 1774–1791.
[4] I. Basu, T. Al-Samman, G. Gottstein, Mater Sci Eng A 579 (2013) 50–56.
[5] I. Basu, T. Al-Samman, Acta Mater 67 (2014) 116–133.
[6] C.W. Su, L. Lu, M.O. Lai, Philos Mag 88 (2) (2008) 181–200.
[7] Q. Li, G.J. Huang, X.D. Huang, S.W. Pan, C.L. Tan, Q. Liu, J Magnes Alloy 5 (2) (2017) 166–172.
[8] M. Yang, H.-L. Jia, R. Jiang, X.-L. Zhou, P.-K. Ma, Z.-G. Li, M. Zha, H.-Y. Wang, J Magnes Alloy (2024).
[9] F.J. Humphreys, M. Hatherly, Recrystallization and related annealing phenomena, 2nd ed., Pergamon Press, Oxford, 2004.
[10] C. Zheng, S. Chen, M. Cheng, S. Zhang, Y. Li, Y. Yang, J. Magnes. Alloy. 11 (11) (2023) 4218–4234.
[11] M. Guillope, J.P. Poirier, J Geophys Res 84 (NB10) (1979) 5557–5567.
[12] P. Du, S. Furusawa, T. Furushima, J Magnes Alloy 10 (3) (2022) 730–742.
[13] P.R. Rios, F. Siciliano Jr, H.R.Z. Sandim, R.L. Plaut, A.F. Padilha, Mater Res 8 (2005) 225–238.
[14] A.E. Smith, Surf Sci 601 (24) (2007) 5762–5765.
[15] D. Cram, H. Zurob, Y. Bréchet, C. Hutchinson, Mater Sci Forum 715-716 (2012) 492–497.
[16] O. Sitdikov, R. Kaibyshev, Mater Trans 42 (9) (2001) 1928–1937.
[17] R. Kaibyshev, in: C. Bettles, M. Barnett (Eds.), Advances in wrought magnesium alloys, Woodhead Publishing, Cambridge, England, 2012, pp. 186–225. https://doi.org/10.1533/9780857093844.1.186.
[18] A. Galiyev, R. Kaibyshev, G. Gottstein, Acta Mater 49 (7) (2001) 1199–1207.
[19] R. Pei, Y. Zou, M. Zubair, D. Wei, T. Al-Samman, Acta Mater 233 (2022) 117990.
[20] R. Hielscher, H. Schaeben, J Appl Crystallogr 41 (6) (2008) 1024–1037.
[21] R. Pei, S. Korte-Kerzel, T. Al-Samman, Mater Sci Eng A 763 (2019) 138112.
[22] R. Pei, Y. Zou, D. Wei, T. Al-Samman, Acta Mater 208 (2021) 116749.
[23] M.A. Lopez-Sanchez, A. Tommasi, F. Barou, R. Quey, Mater Charact 165 (2020) 110382.
[24] K. Higashida, J. Takamura, N. Narita, Mater Sci Eng 81 (1986) 239–258 https://doi.org/10.1016/0025-5416(86)90266-1.
[25] R.W.K. Honeycombe, J Institut Metals 80 (2) (1951) 45–49.
[26] K. Kashihara, M. Tagami, F. Inoko, Materials Transact Jim 37 (4) (1996) 564–571.
[27] Y. Tang, J.A. El-Awady, Acta Mater 71 (2014) 319–332.
[28] Y. Zhu, D. Hou, K. Chen, Z. Wang, J Magnes Alloy 11 (10) (2023) 3634–3641.
[29] S.H. Kim, S.W. Bae, S.W. Lee, B.G. Moon, H.S. Kim, Y.M. Kim, J. Yoon, S.H. Park, Mater Sci Eng A 725 (2018) 309–318.
[30] C. Jun, Z. Qing, L.I. Quan-an, J Alloys Compd 686 (2016) 375–383.
[31] S.R. Agnew, O. Duygulu, Int J Plast 21 (6) (2005) 1161–1193.
[32] S.R. Agnew, M.H. Yoo, C.N. Tome, Acta Mater 49 (20) (2001) 4277–4289.
[33] T. Nogaret, W.A. Curtin, J.A. Yasi, L.G. Hector, D.R. Trinkle, Acta Mater 58 (13) (2010) 4332–4343.
[34] H. Wang, J. Guénolé, S. Korte-Kerzel, T. Al-Samman, Z. Xie, Computation Mater Sci 240 (2024) 113025.
[35] Z. Wu, R. Ahmad, B. Yin, S. Sandlöbes, W.A. Curtin, Science 359 (6374) (2018) 447–452.
[36] B. Syed, J. Geng, R.K. Mishra, K.S. Kumar, Scripta Mater 67 (7) (2012) 700–703.
[37] K.Y. Xie, Z. Alam, A. Caffee, K.J. Hemker, Scripta Mater 112 (2016) 75–78.
[38] T. Obara, H. Yoshinga, S. Morozumi, Acta Metal 21 (7) (1973) 845–853.
[39] S. Sandlöbes, M. Friák, S. Zaefferer, A. Dick, S. Yi, D. Letzig, Z. Pei, L.F. Zhu, J. Neugebauer, D. Raabe, Acta Mater 60 (6) (2012) 3011–3021.
[40] S. Sandlöbes, M. Friák, J. Neugebauer, D. Raabe, Mater Sci Eng A 576 (2013) 61–68.
[41] S. Sandloebes, S. Zaefferer, I. Schestakow, S. Yi, R. Gonzalez-Martinez, Acta Mater 59 (2) (2011) 429–439.
[42] Y. Yang, F. Liu, K. Chen, B. Liu, Z. Shan, B. Li, J Magnes Alloy 11 (12) (2023) 4498–4512.
[43] M. Stipp, H. Stunitz, R. Heilbronner, S.M. Schmid, J Struct Geol 24 (12) (2002) 1861–1884.
[44] S.E. Ion, F.J. Humphreys, S.H. White, Acta Metal 30 (10) (1982) 1909–1919.